Chapter 5

Band splitting induced Berry flux and intrinsic anomalous Hall conductivity in NiCoMnGa quaternary Heusler compound

This work is authored by Gaurav K. Shukla et al. and published in Phys. Rev. B 106, 045131 (2022).

In this chapter, the study anomalous Hall effect (AHE) in NiCoMnGa is conducted to understand how magnetization and topological band structure impact the AHE. NiCoMnGa compound whose magnetic moment is comparable to the well-known high AHC compound Co_2MnGa, however, it has no relevant mirror symmetry planes in contrast to the full Heusler compound resulting in the absence of nodal lines. The calculated AHC of NiCoMnGa is approximately ten times lower than that of Co_2MnGa, despite both materials exhibiting nearly close magnetic moments. The lower AHC in NiCoMnGa in comparison to the Co_2MnGa is related to the absence of nodal lines in the band structure of NiCoMnGa.

5.1 Introduction

The anomalous Hall effect (AHE) originates in the ferromagnetic materials due to the interplay between magnetism and spin-orbit coupling (SOC) [1, 2]. In the initial phase of research on AHE, Kundt et.al found that the Hall resistivity in the ferromagnetic material is roughly proportional to the magnetization of the materials [3]. However, the later discovery of the intrinsic origin of AHE revolutionized the understanding of the AHE [4–6]. The intrinsic mechanism emphasizes that the Berry curvature associated with the band structure gives the large AHE [7]. The magnetic moment of the system breaks the time-reversal symmetry and the Berry curvature which acts as a pseudomagnetic field in the reciprocal space deflects the electron in the transverse direction [8, 9]. In real materials, the Berry curvature is finite when two or more bands approach each other energetically and hybridize [9]. The symmetry of the crystal brings the spin bands closer and SOC allows them to hybridize [9]. The SOC has small energy in comparison to the exchange splitting energy of ferromagnets, however, the small energy of SOC can split the band dispersion near the Fermi energy and when the Fermi energy lies in the SOC energy gap, a non-zero dissipationless Hall current arises due to non-vanishing total flux of Berry curvature [10, 11]. Several materials have been reported to have large intrinsic AHC due to the Berry curvature originating from their characteristic spin-orbit coupled band structure. For example, the intrinsic AHC in Fe (751 S/cm) [11] and MnAs ($\sim 10^3$ S/cm) [10] have been reported due to the Berry curvature arising from a pair of spin-orbit coupled band near to the Fermi level. $Co_3Sn_2S_2$ [12], Fe_3Sn [13] and $LiMn_6Sn_6$ [14] show the large intrinsic AHC arising due to the finite Berry curvature associated with the band structure. Besides these materials, Heusler alloys [15–17] show the exotic anomalous transport properties owing to the distinctive band structure due to the combined effect of SOC and broken time-reversal symmetry [18–21]. For example, Co_2MnAl [22], Co_2MnGa [19], Fe_2-based Heusler alloys [23] show the large intrinsic AHE. In this chapter, we have discussed that the Berry curvature plays a crucial role in determining the AHE in the material and the magnetic moment breaks the time-reversal symmetry to avoid the cancellation of AHE.

Co_2MnGa is a full Heusler compound that crystallizes in the $L2_1$ structure with space group $Fm\bar{3}m$, consists of three nodal lines near Fermi energy, derived from the three mirror symmetries present in the system in the absence of SOC [24]. With the consideration of SOC, these nodal lines gap out according to the magnetization direction and create the large Berry curvature and intrinsic AHE in the system [21, 24]. In this work, we studied the AHE in NiCoMnGa quaternary Heusler compound, which can be obtained by replacing the one Co atom with its neighboring Ni atom in Co_2MnGa full Heusler compound keeping the magnetic moments nearly close for both the compounds. Experimentally, we found the value of AHC around 256 S/cm at 10K with an intrinsic contribution of $\sim$ 121 S/cm. The theoretical calculations give the intrinsic AHC $\sim$ 100 S/cm, which is in good agreement with the experiment. The reduction of the mirror symmetries in the NiCoMnGa in comparison to the Co_2MnGa leads to the absence of a nodal line, nevertheless, the band splitting in the presence of SOC at Fermi energy leads to the finite Berry curvature and intrinsic AHC in the system.

5.2 Methods

Polycrystalline NiCoMnGa Heusler compound was synthesized by arc melting method in the environment of high pure argon atmosphere by taking 99.99 % pure constituent elements in the water-cooled copper hearth. A Ti piece was used as an oxygen getter to reduce further contamination. The sample was flipped several times and re-melted for homogeneous mixing. For the structural analysis x-ray diffraction (XRD) pattern of the powder sample was recorded at room temperature using a Rigaku-made x-ray diffractometer with Cu-K_α radiation. The magnetization measurements were performed using a vibrating sample magnetometer (VSM) attached to the Physical Properties Measurement System (PPMS) from Quantum Design. The resistivity and Hall measurement were carried out on a rectangular piece of the sample of dimension $4.34 \times 2.45 \times 0.66$ mm^3 employing four-probe method using Cryogen Free Measurement System (CFMS). The electronic band structure and magnetic properties of the NiCoMnGa were calculated by employing density functional theory (DFT) using the Vienna ab initio simulation package (VASP) [25]. The generalized gradient approximation (GGA) of the Perdew-Burke-Ernzerhof (PBE) type was used for the exchange-correlation functional [26]. The kinetic energy cutoff of 520 eV was taken for the plane-wave basis. A $15 \times 15 \times 15$ k-point mesh was used for the Brillouin zone (BZ) sampling and the Gaussian smearing method with a width of 0.1 eV was adopted for the Fermi surface broadening. The cell parameter was relaxed until the forces on all atoms were smaller than 0.01 eV/Å. The SOC was taken into account in all the calculations. To explore the non-trivial band topology and the intrinsic AHC, the tight binding Hamiltonian was constructed with the maximally localized Wannier functions using the Wannier90 code [27, 28]. Based on the tight-binding Hamiltonian, the AHC and the Berry curvature were evaluated via the Kubo-formula approach [29].

5.3 Result and discussion

5.3.1 Structure and magnetization

The XRD pattern of NiCoMnGa was recorded at room temperature for structural analysis. The observed XRD pattern (red curve in Fig. 5.1(a)) fairly shows the cubic structure of the sample. The quaternary Heusler alloys generally crystallize in the LiMgPdSn type structure (space group $F\bar{4}3m$)[30]. The Rietveld refinement of the room temperature XRD pattern of NiCoMnGa was carried out using FULLPROF software package [31] in the space group of $F\bar{4}3m$ (space group no.216) and the special Wyckoff's positions; 4d (0.75,0.75,0.75), 4c (0.25, 0.25,0.25,0.25), 4b (0.5, 0.5, 0.5), and 4a (0, 0, 0) were considered for Nickel (Ni), Cobalt(Co), Manganese (Mn) and Gallium (Ga) atoms, respectively. The calculated XRD pattern (black curve) depicted in Fig. 5.1(a), shows that all the Bragg peaks are well-indexed, which confirms the single-phase (cubic) of the sample. The refined lattice parameter was found 5.79 Å, which matches well with the value reported in the literature [32]. The presence of the (111) and (200) superlattice reflections generally mark the ordered structure of Heusler compounds [18]. For NiCoMnGa the structure factors for (111), (200),

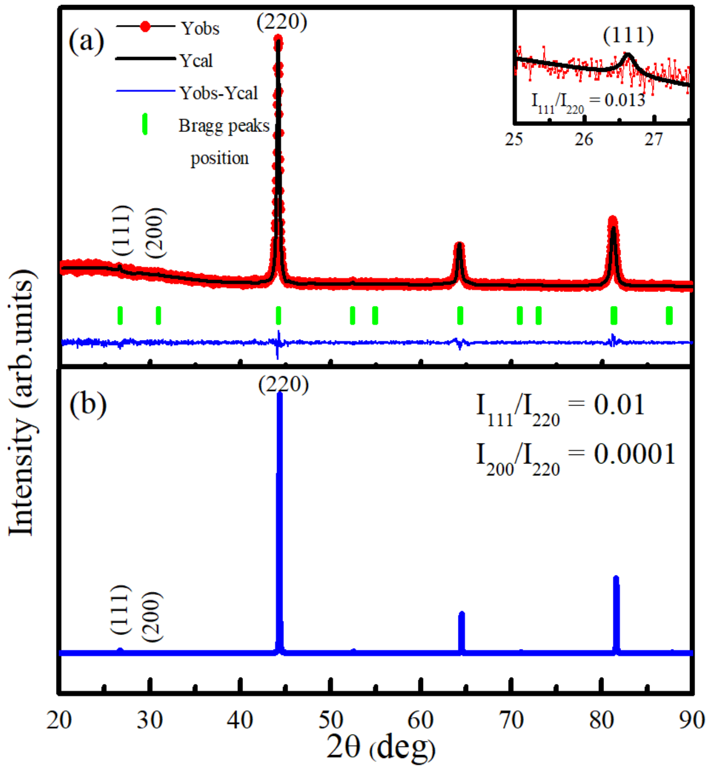

Figure 5.1: Rietveld refinement of the room temperature powder x-ray diffraction (XRD) data of NiCoMnGa system. The inset shows an enlarged view of XRD pattern around (111) superlattice reflection. (b) Simulated XRD pattern of NiCoMnGa system.

and (220) reflections can be written as [33]

$$F_{111} = 4[(f_{Ga} - f_{Mn}) - i(f_{Ni} - f_{Co})] \tag{5.1}$$

$$F_{200} = 4[(f_{Ga} + f_{Mn}) - (f_{Ni} + f_{Co})] \tag{5.2}$$

$$F_{220} = 4[(f_{Ga} + f_{Mn}) + (f_{Ni} + f_{Co})] \tag{5.3}$$

The negligible intensity of the (111) superlattice reflection survives only due to the difference of the atomic scattering factors (SFs) of Ga and Mn atoms as the difference between atomic SFs of Ni and Co atoms is negligible (both are the consecutive elements in the periodic table) [18, 33]. The vanishing intensity of the (200) reflection can be understood from Eq.5.2. The intensity of fundamental reflection is due to the sum of all atomic SFs of constituent elements (Eq.5.3). We simulated the XRD pattern of NiCoMnGa using POWDERCELL software [34] depicted in Fig. 5.1(b). The intensity ratio of superlattice reflection (111) to the fundamental reflection (220) (*i.e.* $\frac{I_{111}}{I_{220}}$) was found about 0.01 and 0.012 from the simulated and observed XRD patterns, which suggests the formation of the ordered structure of NiCoMnGa Heusler compound. Inset of Fig. 5.1(a) shows the enlarged view of the XRD pattern around (111) superlattice reflection. Since the ordered structure of this compound has not been clarified, there is a possibility of Co-Ni disorder as XRD has limitations in detecting disorder within the material containing the elements of similar atomic SFs. Figure 5.2 shows the magnetic isotherms at the temperatures 10 K and 300 K. The magnetic moment was found 4.7 μ_B/f.u at 10 K. The magnitude of the observed magnetic moment is close to the value reported in literature[32].

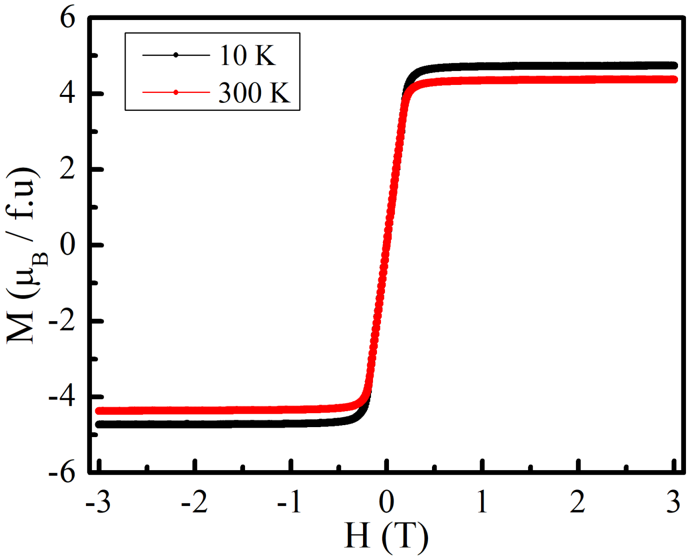

Figure 5.2: Field-dependent magnetic isotherms at 10 K and 300 K.

5.3.2 Transport measurements

Figure 5.3(a) shows the measured temperature dependence of longitudinal resistivity (ρ_{xx}). The temperature variation of ρ_{xx} indicates the metallic conduction with σ_{xx} about 1.88×10^4 S/cm at 300 K. The residual resistance ratio (RRR= $\rho_{\mathrm{xx}}(300K)/\rho_{\mathrm{xx}}(10K)$), which quantifies the degree of disorder, is found around 2, which suggests a clean sample of NiCoMnGa [18]. Now, afterward investigating the phase purity, magnetization, and resistivity of the sample, we will discuss the outcomes of Hall measurement. Inset of Fig. 5.3(a) shows the schematic diagram of the sample device used for longitudinal voltage (V_{xx}) and Hall voltage (V_H) measurements. In general the Hall resistivity (ρ_H)

in magnetic materials is sum of two parts [1, 18];

$$\rho_H = \rho_H^0 + \rho_H^A = R_0 H + R_s M \tag{5.4}$$

ρ_H^0 and ρ_H^A are the ordinary and anomalous Hall resistivity, respectively. R_0, R_s, H, and M are the ordinary Hall coefficient, anomalous Hall coefficients, applied external magnetic field, and spontaneous magnetization of material, respectively. R_0 which depends on the type of charge carriers and their density is the inverse of the product of carrier concentration (n) and electronic charge (e) [35]. The Hall resistivity in ferromagnetic materials is dominated by AHE at the lower field and the role of the ordinary Hall effect usually appears in the higher field region [18]. With the linear fitting of the high field ρ_H curve, slope and intercept on the y-axis give R_0 and ρ_H^A, respectively. ρ_H^A is similar to Hall response due to the magnetization of a material in the absence of an external magnetic field. Hall measurement outcomes are summarized in Fig. 5.3 (b)-(f) and Fig. 5.4 (a)-(b). Figure 5.3(b) shows the field dependent ρ_H isotherms up to field of 4 T. The ρ_H curves show a sharp jump at the low field and change linearly in the high field regime signifies an AHE in the present material. Figure 5.3(c) displays the variation of extracted ρ_H^A with temperature. ρ_H^A increases non-linearly with temperature and achieves the maximum value of about 0.56 $\mu\Omega$-cm at room temperature. We also measured the field-dependent ρ_{xx} at fixed temperatures. The ρ_{xx} does not change significantly with the magnetic field at a particular temperature as shown in the inset of Fig. 5.3(c) for (i) 10 K, (ii) 200 K, and (iii) 300 K. The charge carrier density (n) was calculated using relation $R_0 = \frac{1}{ne}$ [35] and temperature variation of n is depicted in Fig. 5.3(d). The magnitude of n is a little scattered with temperature and estimated about 2.5×10^{21} cm^{-3} at 300 K. To examine the origin of AHE, we have plotted the ρ_H^A versus ρ_{xx} on a double logarithmic scale as shown in Fig. 5.3(e). A linear fitting was done to determine the exponent α according to the formula $\rho_H^A \propto \rho_{xx}^\alpha$ [35, 36]. If $\alpha = 1$, the origin of AHE is due to skew scattering, and if $\alpha = 2$, the origin of AHE is assigned to the intrinsic and side jump mechanisms [2, 18, 36]. In this way, we found the exponent $\alpha = 1.50$, which primarily specifies that the extrinsic and intrinsic mechanisms are involved in the AHE. To disentangle the intrinsic and extrinsic contributions linked with AHE, we have used the following equation, which accounts

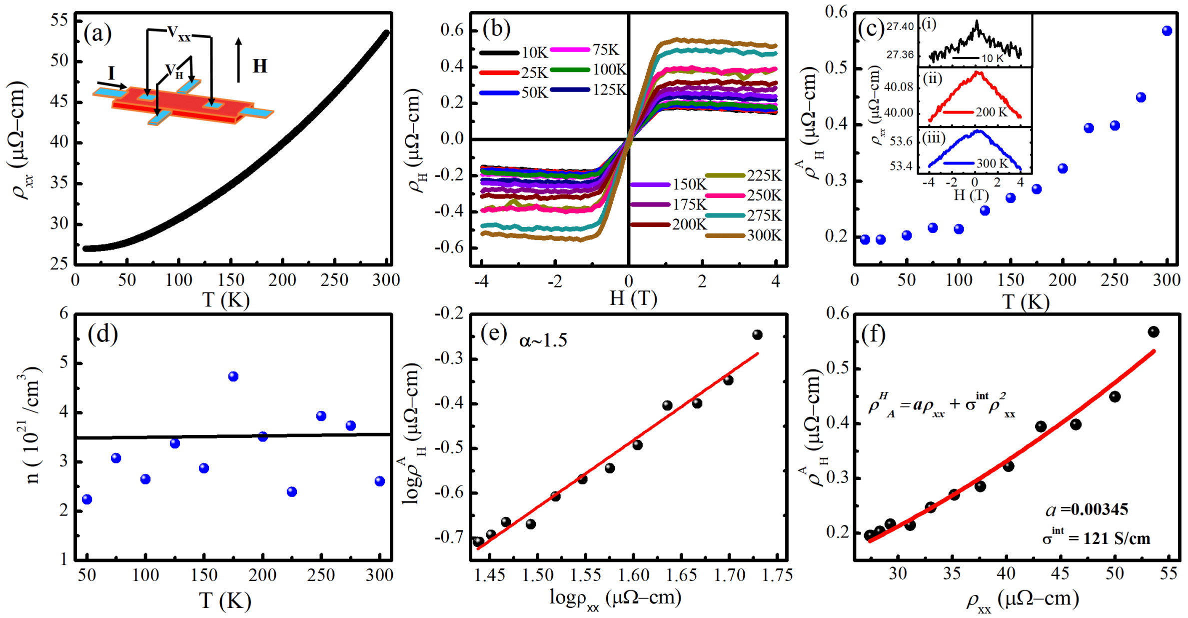

Figure 5.3: (a) Temperature-dependent longitudinal resistivity ρ_{xx}. The inset shows a schematic drawing of a sample device used for Hall voltage V_H and longitudinal voltage V_{xx} measurements. (b) Field-dependent Hall resistivity ρ_H at different temperatures. (c) Temperature variation of anomalous Hall resistivity ρ^A_H. Inset shows the field-dependent ρ_{xx} at (i) 10 K, (ii) 200 K, and (iii) 300 K. (d) Temperature-dependent carrier concentration n. (e) Double logarithmic plot between ρ^A_H and ρ_{xx} (black balls) and the linear fitting is shown by a red line. (f) ρ^A_H and ρ_{xx} plot (black balls) and fitted curve using Eq.5.5 is shown in red color .

for the phonon contribution in the skew scattering as suggested for alloys system [18, 35, 37, 38]

$$\rho^A_H = a\rho_{xx} + \sigma^{int}\rho^2_{xx}. \tag{5.5}$$

Here a is the parameter related to the skew scattering and the notation σ^{int} is used for intrinsic AHC. Here we have assumed the ratio of SOC energy (ϵ_{SO}) to the Fermi energy (E_F) *i.e.* ϵ_{SO}/E_F is in order of 10^{-3} to 10^{-2}, which leads the suppression of side jump contribution in comparison to intrinsic AHC as observed for other metallic ferromagnets [18, 36]. Fig. 5.3(f) shows the ρ^A_H versus ρ_{xx} plot (black balls) and the fitting was employed using Eq.5.5 as shown by a red curve. From fitting, the parameter a and σ^{int} comes out to be 0.0034 and 121 S/cm, respectively. The change in σ^A_H with temperature and/or longitudinal conductivity (σ_{xx}) also holds the information about the involved mechanism in the AHE. Hall conductivity (σ_H) was calculated using equation [18, 24, 39]

$$\sigma_H = \frac{\rho_H}{(\rho^2_{xx} + \rho^2_H)} \tag{5.6}$$

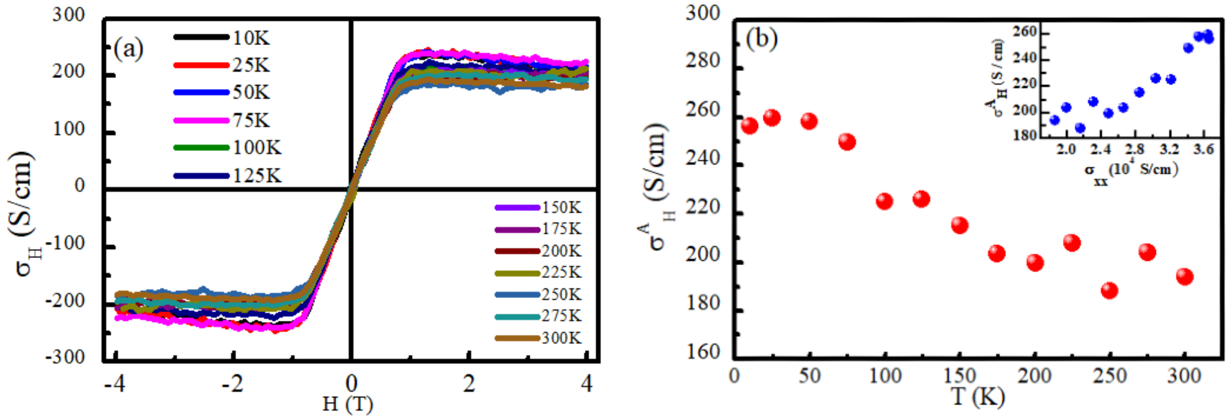

Figure 5.4: (a) Field-dependent Hall conductivity σ_H at different temperatures. (b) Temperature variation of anomalous Hall conductivity (AHC). Inset shows the variation of AHC with longitudinal conductivity σ_{xx}.

Figure 5.4 (a) shows the field-dependent Hall conductivity curves at different temperatures. The value of AHC at a particular temperature is calculated by zero-field extrapolation of the high-field Hall conductivity data with the y-axis. We found the AHC around 256 S/cm at 10 K. This value is nearly twice of the magnitude of the intrinsic AHC, which shows the presence of equal contribution of intrinsic and extrinsic AHC at 10 K. The AHC decreases with increasing the temperature and reduces to 194 S/cm at 300 K as shown in Fig. 5.4(b). The variation of AHC with σ_{xx} is shown in the inset of Fig. 5.4(b). The decreasing (increasing) value of AHC with temperature (σ_{xx}) is due to the skew scattering contribution in AHC rather than the temperature variation of spontaneous magnetization of sample as the temperature has a little effect on the magnetization of the present system (Fig. 5.2). It is worthwhile to mention here that intrinsic AHE is expected to dominate in the overall behavior of AHE, when the longitudinal conductivity of the sample lies in the good metallic regime *i.e.* σ_{xx} is an order of 10^4-10^6 S/cm [1, 18, 36, 39, 40]. Our system shows the deviation from this criterion as the extrinsic AHE has a significant contribution in the AHE despite the σ_{xx} is an order of 10^4 S/cm. The AHC due to skew scattering can be given as [41]

$$\sigma_H^{skew} = \sigma_{xx} S = \frac{2e^2}{ha}\frac{E_F\tau}{\hbar}S \tag{5.7}$$

where h, a, E_F, τ and S are the Planck constant, lattice parameter, Fermi energy, mean free path of electron, and skewness factor, respectively. The skewness factor is S $\sim \epsilon_{SO}$v$_{imp}$/W^2, where W is the bandwidth and v$_{imp}$ is impurity potential [41]. In the superclean limit where the $\frac{\hbar}{\tau} << \epsilon_{SO}$, the skew scattering dominates, however in the case of $\frac{\hbar}{\tau}$ $<\epsilon_{SO}$, the skew scattering contribution decreases. From Eq.5.7, it is clear that the skew scattering contribution rapidly decays with increasing the $\frac{\hbar}{\tau}$. Henceforth, the value of AHC due to skew scattering depends on both the strength of SOC energy and the σ_{xx}. Our experiment also suggests that the lineup of the origin of AHE based solely on the longitudinal conductivity is a rough estimation and need not be strictly valid. Since the intrinsic AHE depends on the Berry curvature of the system, which may have different origins such as the presence of a gapped nodal line, Weyl point, or interband mixing along a certain high symmetry path. Therefore, to understand the origin of Berry curvature in the present system, we performed the first principles calculation.

5.3.3 First principles calculation

The relaxed lattice parameter of NiCoMnGa was found 5.782 Å, which is consistent with the experiment. Our first-principles calculation for a magnetic moment suggests that Co and Mn have a large magnetic moment with μ_{Co}=1.188 μ_B/f.u and μ_{Mn}=3.246 μ_B/f.u respectively, whereas Ga has a small vanishing magnetic moment and Ni have a moment μ_{Ni}=0.563 μ_B/f.u. The total magnetic moment per formula unit is 4.993 μ_B, aligned along the (001) direction, which is consistent with the Slater Pauling rule for Heusler alloys [42]. To calculate the Berry curvature and the intrinsic AHE in the present system, the tight-binding Hamiltonian was constructed with the maximally localized Wannier functions [27, 28]. Based on the tight-binding Hamiltonian, the AHC and the Berry curvature were evaluated using the Kubo formula [29]. The intrinsic AHE can be analyzed by exploring the electronic band structure of the NiCoMnGa. Two major features in electronic band structure make this system important; first, a twofold degenerate band forms a triple point crossing with a non-degenerate band along high symmetry direction Γ-L in the absence of SOC as shown in Fig. 5.5(a) by a black dotted circle. This doubly degenerate band splits in the presence of SOC and also lifts the triple-point degeneracy. This degeneracy may arise due to a symmetry of C_{3v} along Γ-L high symmetry direction, whose elements are threefold rotation (C_3) and a σ_v mirror plane [43]. The second feature is a pair of degenerate minority spin bands at Γ point in the absence of SOC, however, in the presence of SOC these bands split into an occupied and an unoccupied band separated by a small energy gap in a small k interval near Γ point as shown in Fig. 5.5(b). In Fig. 5.5(d),

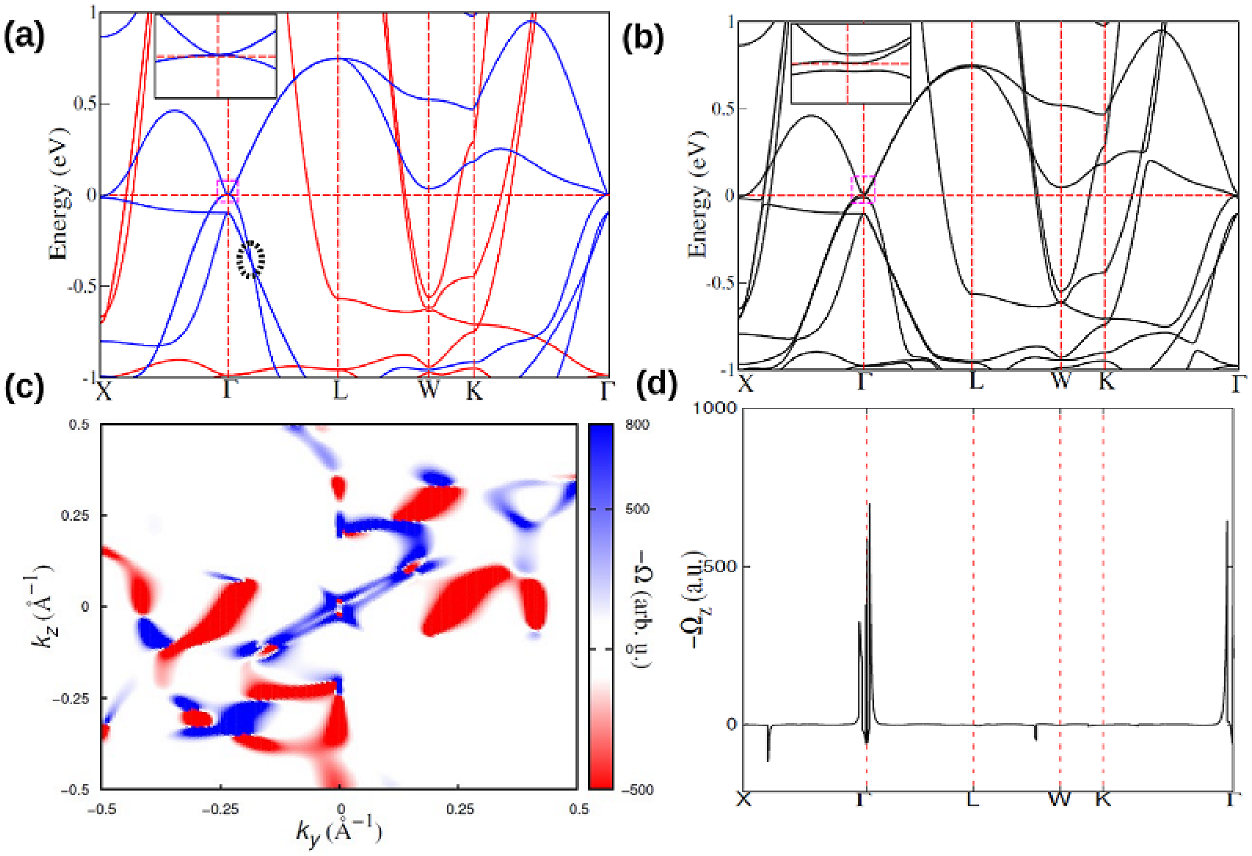

Figure 5.5: (a) The band structure of NiCoMnGa in the absence of SOC, where the red and blue colors represent the spin-up and spin-down bands, respectively. (b) The band structure of NiCoMnGa in the presence of SOC. The inset shows the splitting of the bands near the Fermi energy E_F. (c) Berry curvature distribution in k_y-k_z plane at $k_x = 0$. (d) Berry curvature along the high-symmetry path.

we calculated the Berry curvature Ω^z_{xy} in the presence of SOC along the same symmetry direction and Ω^z_{xy} has a large value near the Γ point. This large value of Berry curvature can be explained in terms of the splitting of the degenerate band, which opens a small energy gap and creates intrinsic AHC in the system. Owing to the nearly degenerate conduction and valance band at Γ point, the Berry curvature is large at this point; therefore an intrinsic AHE is expected in the present compound. In Fig. 5.5(c), the color plot of Berry curvature is shown in k_x =0 plane of the first Brillouin zone, which shows the positive and negative distribution of Berry curvature in the plane. Following the symmetry of the NiCoMnGa compound, if the magnetization is taken along the z-axis, Ω^z_{xy} is the only survival component of the Berry curvature. We found the intrinsic AHC due to finite Ω^z_{xy} about 100 S/cm at the Fermi level, which is consistent with the experiment (121 S/cm). We also showed the dependency of AHC as a function of the shift in Fermi energy in Fig. 5.6, which gives

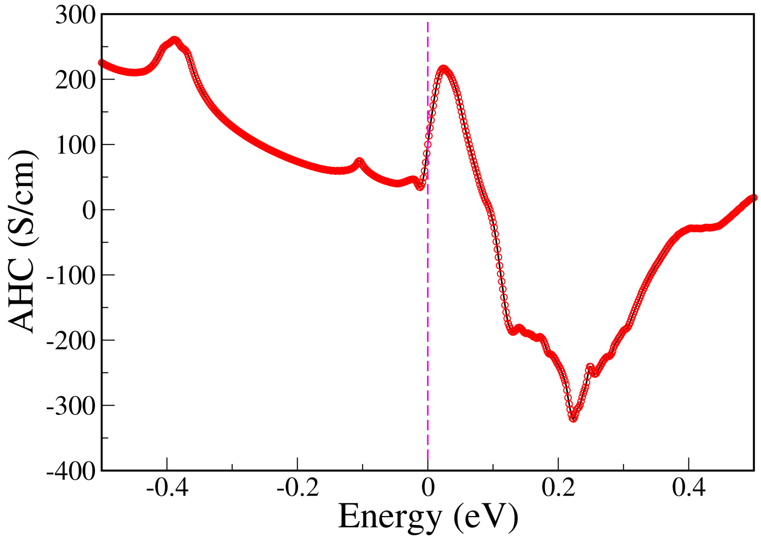

Figure 5.6: Fermi energy scan of the anomalous Hall conductivity.

an idea about the contribution of various valance bands by shifting the Fermi energy. The large peak below the Fermi level (-0.38 eV) is due to the large Berry curvature at the triple point, which is contributing as an occupied valence band to AHC. We observed the decreasing trend of AHC from -0.38 eV and it again increases at Fermi energy due to a large positive Berry curvature shown by the blue color in Fig. 5.5(c).

5.4 Conclusion

We have experimentally measured the AHC in the NiCoMnGa quaternary Heusler compound and theoretically calculated the intrinsic part of the AHC due to the Berry curvature of the dispersion bands. The extrinsic and intrinsic mechanisms contribute equally to the AHC of the present system. We found a good agreement between the experimentally extracted intrinsic AHC and the theoretically calculated AHC. The reduction of the number of mirror symmetries in NiCoMnGa in comparison to Co_2MnGa leads to the absence of nodal lines; nevertheless, the band splitting in the presence of SOC at the Fermi energy leads to the finite Berry curvature and intrinsic AHC in the system. The presence of a significant contribution of the extrinsic mechanism in the AHE, despite the longitudinal conductivity being of the order of 10^4 S/cm, suggests that the relation of the origin of the AHE solely with the longitudinal conductivity may not be strictly valid.

References

[1] N. Nagaosa, Anomalous Hall effect—A new perspective, J. Phys. Soc. Jpn. **75**, 042001 (2006).

[2] N. Nagaosa, J. Sinova, S. Onoda, A. H. MacDonald, and N. P. Ong, Anomalous Hall effect, Rev. Mod. Phys. **82**, 1539 (2010).

[3] A. Kundt, On the Hall effect in ferromagnetic materials, Wied. Ann **49**, 257 (1893).

[4] J. Smit, The spontaneous Hall effect in ferromagnetics I, Physica **21**, 877 (1955).

[5] J. Smit, The spontaneous Hall effect in ferromagnetics II, Physica **24**, 39 (1958).

[6] R. Karplus and J. Luttinger, Hall effect in ferromagnetics, Phys. Rev. **95**, 1154 (1954).

[7] D. Xiao, M.-C. Chang, and Q. Niu, Berry phase effects on electronic properties, Rev. Mod. Phys. **82**, 1959 (2010).

[8] K. Manna, Y. Sun, L. Muechler, J. Kübler, and C. Felser, Heusler, Weyl and Berry, Nat Rev Mater **3**, 244 (2018).

[9] O. Stejskal, M. Veis, and J. Hamrle, The flow of the Berry curvature vector field, Sci. Rep. **12**, 97 (2022).

[10] C. Helman, A. Camjayi, E. Islam, M. Akabori, L. Thevenard, C. Gourdon, and M. Tortarolo, Anomalous Hall effect in MnAs: Intrinsic contribution due to Berry curvature, Phys. Rev. B **103**, 134408 (2021).

[11] Y. Yao, L. Kleinman, A. H. MacDonald, J. Sinova, T. Jungwirth, D.-s. Wang, E. Wang, and Q. Niu, First principles calculation of anomalous Hall conductivity in ferromagnetic bcc Fe, Phys. Rev. Lett. **92**, 037204 (2004).

[12] E. Liu, Y. Sun, N. Kumar, L. Muechler, A. Sun, L. Jiao, S.-Y. Yang, D. Liu, A. Liang, Q. Xu, *et al.*, Giant anomalous Hall effect in a ferromagnetic kagome-lattice semimetal, Nat. Phys **14**, 1125 (2018).

[13] T. Chen, S. Minami, A. Sakai, Y. Wang, Z. Feng, T. Nomoto, M. Hirayama, R. Ishii, T. Ko-

retsune, R. Arita, and S. Nakatsuji, Large anomalous Nernst effect and nodal plane in an iron-based kagome ferromagnet, Sci. Adv. **8**, eabk1480 (2022).

[14] D. Chen, C. Le, C. Fu, H. Lin, W. Schnelle, Y. Sun, and C. Felser, Large anomalous Hall effect in the kagome ferromagnet $LiMn_6Sn_6$, Phys. Rev. B **103**, 144410 (2021).

[15] L. Wollmann, A. K. Nayak, S. S. Parkin, and C. Felser, Heusler 4.0: tunable materials, Annu. Rev. Mater. Res. **47**, 247 (2017).

[16] T. Graf, C. Felser, and S. S. Parkin, Simple rules for the understanding of Heusler compounds, Prog. Solid. State Ch. **39**, 1 (2011).

[17] K. Elphick, W. Frost, M. Samiepour, T. Kubota, K. Takanashi, H. Sukegawa, S. Mitani, and A. Hirohata, Heusler alloys for spintronic devices: review on recent development and future perspectives, Sci. Technol. Adv. Mater. **22**, 235 (2021).

[18] G. K. Shukla, J. Sau, N. Shahi, A. K. Singh, M. Kumar, and S. Singh, Anomalous Hall effect from gapped nodal line in the Co_2FeGe Heusler compound, Phys. Rev. B **104**, 195108 (2021).

[19] K. Manna, L. Muechler, T.-H. Kao, R. Stinshoff, Y. Zhang, J. Gooth, N. Kumar, G. Kreiner, K. Koepernik, R. Car, J. Kübler, G.H. Fecher, C. Shekhar, Y. Sun, and C. Felser, From colossal to zero: controlling the anomalous Hall effect in magnetic Heusler compounds via Berry curvature design, Phys. Rev. X **8**, 041045 (2018).

[20] S.-Y. Xu, I. Belopolski, N. Alidoust, M. Neupane, G. Bian, C. Zhang, R. Sankar, G. Chang, Z. Yuan, C.-C. Lee, S.-M. Huang, H. Zheng, J. Ma, D. S. Sanchez, B. Wang, A. Bansil, F. Chou, P. P. Shibayev, H. Lin, S. Jia, and M. Zahid Hasan, Discovery of a Weyl Fermion semimetal and topological Fermi arcs, Science **349**, 613 (2015) .

[21] I. Belopolski, K. Manna, D. S. Sanchez, G. Chang, B. Ernst, J. Yin, S. S. Zhang, T. Cochran, N. Shumiya, H. Zheng, B. Singh,G. Bian, D. Multer, M. Litskevich, X. Zhou, S. M. Huang, B. Wang, T.R. Chang, S.-Y. Xu, A. Bansal, C. Felser, H. Lin, and M. Zahid Hasan, Discovery of topological Weyl Fermion lines and drumhead surface states in a room temperature magnet, Science **365**, 1278 (2019).

[22] P. Li, J. Koo, W. Ning, J. Li, L. Miao, L. Min, Y. Zhu, Y. Wang, N. Alem, C.-X. Liu, Z.

Mao, and B. Yan, Giant room temperature anomalous Hall effect and tunable topology in a ferromagnetic topological semimetal Co_2MnAl, Nat. Commun. **11**, 3476 (2020).

[23] F. Mende, J. Noky, S. N. Guin, G. H. Fecher, K. Manna, P. Adler, W. Schnelle, Y. Sun, C. Fu, and C. Felser, Large anomalous Hall and Nernst effects in high Curie-temperature iron-based Heusler compounds, Adv. Sci. **8**, 2100782 (2021).

[24] S. N. Guin, K. Manna, J. Noky, S. J. Watzman, C. Fu, N. Kumar, W. Schnelle, C. Shekhar, Y. Sun, J. Gooth, and C. Felser, Anomalous Nernst effect beyond the magnetization scaling relation in the ferromagnetic Heusler compound Co_2MnGa, NPG Asia Mater. **11**, 16 (2019).

[25] J. Hafner, Ab-initio simulations of materials using VASP: Density-functional theory and beyond, J. Comput. Chem. **29**, 2044 (2008).

[26] P. E. Blöchl, Projector augmented-wave method, Phys. Rev. B **50**, 17953 (1994).

[27] G. Pizzi, V. Vitale, R. Arita, S. Blügel, F. Freimuth, G. Géranton, M. Gibertini, D. Gresch, C. Johnson, T. Koretsune, J. Ibañez-Azpiroz, H. Lee, J.-M. Lihm, D. Marchand, A. Marrazzo, Y. Mokrousov, J. I. Mustafa, Y. Nohara, Y. Nomura, L. Paulatto, S. Poncé, T. Ponweiser, J. Qiao, F. Thöle, S. S. Tsirkin, M. Wierzbowska, N. Marzari, D. Vanderbilt, I. Souza, A. A. Mostofi, and J. R. Yates, Wannier90 as a community code: New features and applications, J. Condens. Matter Phys. **32**, 165902 (2020).

[28] N. Marzari and D. Vanderbilt, Maximally localized generalized Wannier functions for composite energy bands, Phys. Rev. B **56**, 12847 (1997).

[29] M. Gradhand, D. V. Fedorov, F. Pientka, P. Zahn, I. Mertig, and B. L. Györffy, First-principle calculations of the Berry curvature of Bloch states for charge and spin transport of electrons, J. Condens. Matter Phys. **24**, 213202 (2012).

[30] D. Rani, Enamullah, K. G. Suresh, A. K. Yadav, S. N. Jha, D. Bhattacharyya, M. R. Varma, and A. Alam, Structural, electronic, magnetic, and transport properties of the equiatomic quaternary Heusler alloy CoRhMnGe: Theory and experiment, Phys. Rev. B **96**, 184404 (2017).

[31] J. Rodríguez-Carvajal, FULLPROF, a Rietveld and pattern matching and analysis programs

version 2016, Laboratoire Leon Brillouin, CEA-CNRS, France, http://www.ill.eu/sites/ fullprof/.

[32] V. Alijani, J. Winterlik, G. H. Fecher, S. S. Naghavi, and C. Felser, Quaternary half-metallic Heusler ferromagnets for spintronics applications, Phys. Rev. B **83**, 184428 (2011).

[33] Enamullah, Y. Venkateswara, S. Gupta, M. R. Varma, P. Singh, K. G. Suresh, and A. Alam, Electronic structure, magnetism, and antisite disorder in CoFeCrGe and CoMnCrAl quaternary Heusler alloys, Phys. Rev. B **92**, 224413 (2015).

[34] W. Kraus and G. Nolze, PowderCell-a program for the representation and manipulation of crystal structures and calculation of the resulting x-ray powder patterns, J. Appl. Crystallogr. **29**, 301 (1996).

[35] Q. Wang, Y. Xu, R. Lou, Z. Liu, M. Li, Y. Huang, D. Shen, H. Weng, S. Wang, and H. Lei, Large intrinsic anomalous Hall effect in half-metallic ferromagnet $Co_3Sn_2S_2$ with magnetic Weyl fermions, Nat. commun. **9**, 3681 (2018).

[36] S. Roy, R. Singha, A. Ghosh, A. Pariari, and P. Mandal, Anomalous Hall effect in the half-metallic Heusler compound Co_2TiX (X = Si,Ge), Phys. Rev. B **102**, 085147 (2020).

[37] B. Ernst, R. Sahoo, Y. Sun, J. Nayak, L. Müchler, A. K. Nayak, N. Kumar, J. Gayles, A. Markou, G. H. Fecher, and C. Felser, Anomalous Hall effect and the role of Berry curvature in Co_2TiSn Heusler films, Phys. Rev. B **100**, 054445 (2019).

[38] V. L. Grigoryan, J. Xiao, X. Wang, and K. Xia, Anomalous Hall effect scaling in ferromagnetic thin films, Phys. Rev. B **96**, 144426 (2017).

[39] G. K. Shukla, A. K. Jena, N. Shahi, K. K. Dubey, I. Rajput, S. Baral, K. Yadav, K. Mukherjee, A. Lakhani, K. Carva, S.-C. Lee, S. Bhattacharjee, and S. Singh, Atomic disorder and Berry phase driven anomalous Hall effect in a Co_2FeAl Heusler compound, Phys. Rev. B **105**, 035124 (2022).

[40] M. R. U. Nabi, A. Wegner, F. Wang, Y. Zhu, Y. Guan, A. Fereidouni, K. Pandey, R. Basnet, G. Acharya, H. O. H. Churchill, Z. Mao, and J. Hu, Giant topological Hall effect in centrosymmetric tetragonal $Mn_{2-x}Zn_xSb$, Phys. Rev. B **104**, 174419 (2021).

[41] S. Onoda, N. Sugimoto, and N. Nagaosa, Intrinsic versus extrinsic anomalous Hall effect in ferromagnets, Phys. Rev. Lett. **97**, 126602 (2006).

[42] I. Galanakis, P. H. Dederichs, and N. Papanikolaou, Slater-pauling behavior and origin of the half-metallicity of the full-Heusler alloys, Phys. Rev. B **66**, 174429 (2002).

[43] C. K. Barman, C. Mondal, B. Pathak, and A. Alam, Quaternary Heusler alloy: An ideal platform to realize triple point fermions, Phys. Rev. B **99**, 045144 (2019).